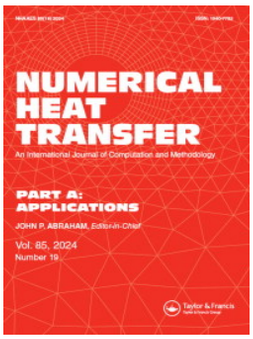

Taylor & Francis
Taylor & Francis Group

Numerical Heat Transfer, Part A: Applications
An International Journal of Computation and Methodology

ISSN: 1040-7782 (Print) 1521-0634 (Online) Journal homepage: www.tandfonline.com/journals/unht20

Cattaneo–Christov double diffusion model for the entropy analysis of a non-Darcian MHD Williamson nanofluid

M. Sagheer, Z. Sajid, S. Hussain & H. Shahzad

To cite this article: M. Sagheer, Z. Sajid, S. Hussain & H. Shahzad (2024) Cattaneo–Christov double diffusion model for the entropy analysis of a non-Darcian MHD Williamson nanofluid, Numerical Heat Transfer, Part A: Applications, 85:19, 3147-3173, DOI: 10.1080/10407782.2024.2380365

To link to this article: https://doi.org/10.1080/10407782.2024.2380365

Published online: 31 Jul 2024.

NUMERICAL HEAT TRANSFER, PART A: APPLICATIONS
2024, VOL. 85, NO. 19, 3147–3173
https://doi.org/10.1080/10407782.2024.2380365

Taylor & Francis
Taylor & Francis Group

Cattaneo–Christov double diffusion model for the entropy analysis of a non-Darcian MHD Williamson nanofluid

M. Sagheer[a], Z. Sajid[a], S. Hussain[b], and H. Shahzad[a]

[a]Department of Mathematics, Capital University of Science and Technology, Islamabad, Pakistan; [b]Institut für Angewandte Mathematik (LS III), Fakultät für Mathematik, Technische Universität Dortmund, Germany

ABSTRACT

This research is carried out to observe the fluid flow across a stratified sheet in the presence of non-linear thermal radiation. Through the process of similarity transformations, the partial differential equations (PDEs) governing the flow model are transformed into ordinary differential equations (ODEs), which are then numerically solved using the shooting method. This study comprehensively examines the influence of various flow parameters, including the inertial coefficient, magnetic parameter, Brownian motion parameter, radiation parameter, Prandtl number, thermophoresis parameter, and Brinkman number, on key thermophysical characteristics, such as the skin friction coefficient, and the rates of heat, mass, and entropy generation. Notably, the relative difference in the skin-friction coefficient increases with the Weissenberg number, ranging from approximately 1.8 to 2.5. The results indicate that reducing the Cattaneo–Christov temperature parameter decreases the temperature profile while increasing the concentration profile, whereas entropy generation initially rises with increasing Weissenberg number, but decreases near the surface.

ARTICLE HISTORY
Received 14 April 2024
Revised 28 June 2024
Accepted 8 July 2024

KEYWORDS
Cattaeno–Christov double diffusion; entropy and magnetohydrodynamics (MHDs); Williamson nanofluid; stratified sheet;

1. Introduction

Fluids, encompassing liquids, gases, and plasma, represent a fundamental phase of matter that undergoes deformation or flow when subjected to external forces [1]. These substances lack a shear modulus, rendering them unable to withstand shear forces. Given their vital role in daily life and natural processes, researchers worldwide are diligently exploring the dynamics of fluid movement. Fluid dynamics investigates fluid flow and its underlying causes, shedding light on phenomena, such as the evolution of stars, ocean currents, tectonic plates, and blood circulation [2]. The practical applications of fluid dynamics are diverse, ranging from wind turbines and oil pipelines to rocket engines and air conditioning systems [3]. The foundational principles of fluid dynamics trace back to Archimedes, who developed the Archimedes principle governing the motion of objects. Fluid mechanics as a field has been under systematic study since the early fifteenth century. Classifying fluids based on the relationship between stress and strain, they are characterized as either Newtonian or non-Newtonian. Non-Newtonian fluids defy Newton's viscosity law, exhibiting nonlinear correlations between

CONTACT S. Hussain shafqat.hussain@math.tu-dortmund.de Institut für Angewandte Mathematik (LS III), Fakultät für Mathematik, Technische Universität Dortmund, Dortmund 44135, Germany

Nomenclature

u, v	Velocity components	N_1	Solutal Stratification parameter
ρ	Density	σ	Electrical conductivity
N_2, N_3	Temperature Ratio	τ	Stress tensor
λ	Porosity constant	b	Stretching constant
ν	Kinematic viscosity	We	Weissenberg number
α	Thermal diffusivity	η	Similarity variable
Nb	Brownian motion parameter	λ_1, λ_2	Time relaxation constant
ρc_p	Heat capacity	D_T	Thermophoresis mass diffusivity
$K*$	Absorption constant	D_B	Brownian motion mass diffusion
K	Thermal conductivity	C_F	Drag coefficient
μ_0	Zero shear rate viscosity	C_∞	Ambient concentration
R	Universal gas constant	γ	Fluid relaxation time
T_∞	Ambient temperature	Br	Brinkman number
$k*$	Permeability of porous medium	L	Diffusion parameter
B_0	Magnetic field constant	X_r, X_b	Cattano-Christov double diffusion parameters
τ_1	Dimensionless temperature gradient		
τ_2	non-dimensional concentration difference	Fr	Inertial coefficients
Le	Lewis number	Nt	Thermophoresis parameter
Pr	Prandtl number	M	Magnetic field parameter
k_1	Chemical reaction parameter	λ_t	Cattaneo–Christov temperature parameter
T	Temperature	λ_d	Cattaneo–Christov concentration parameter
C	Concentration		
Ec	Eckert number		
Rd	Thermal radiation parameter	***Subscript***	
f	Dimensionless parameter	s	Solid particle
$\sigma*$	Satefan Boltzmann constant	f	Fluid
M	Magnetic field parameter		

shear stress and deformation rate. Examples of non-Newtonian fluids include ketchup, paint, blood, shampoo, and mud.

Williamson fluids are distinguished among non-Newtonian fluids for their versatile applications across scientific, technological, and engineering disciplines. These fluids play pivotal roles in material processing, nuclear and chemical industries, bioengineering, and geophysics. They are particularly valuable in scenarios where thermal radiation influences their behavior, enhancing applications in areas such as solar energy capture, advanced material manufacturing, and heat transfer systems. Industries engaged in oil recovery, filtration, polymer engineering, ceramic production, and petroleum extraction rely on sophisticated mathematical models to accurately predict and optimize the complex interplay between Williamson fluid dynamics and thermal radiation effects. The foundational work by Williamson [4] played a pivotal role in understanding the flow characteristics of pseudoplastic materials. In a study conducted by Nadeem *et al.* [5], the observation was made that the dimensionless velocity decreases as the Williamson fluid parameter increases in the context of flow across a stretched surface. Shaheen *et al.* [6] utilized the differential transform method to discuss heat transmission in Williamson fluid flow through a ciliated channel, considering magnetic fields and a porous medium. Furthermore, Obalalu *et al.* [7] employed the Galerkin weighted residual method to explore the effects of chemical reaction, activation energy, and solar radiation on 3-D non-Newtonian fluid flow past an inclined stretching sheet.

Choi [8] introduced the term "nanofluid" to characterize a novel type of fluid formed by combining traditional low thermal conductivity fluids with nanoparticles of sizes smaller than 100 nm. Alternatively, nanofluids can be described as "tiny-sized particles suspended in a base fluid".

Commonly used nanoparticles include carbon nanotubes, carbides, metals, and oxide nanofluids, engineered synthetically to exhibit superior thermal conductivity compared to the conventional fluids. The enhancement of thermal conductivity in nanofluids has been a subject of investigation, with Buongiorno [9] contributing insights into the factors influencing this property. He observed that changes in thermal conductivity result from both the thermophoresis effect and Brownian motion. Nanofluids, owing to their improved thermal properties, find applications as coolants in industries such as heavy vehicles and information technology. Rashid *et al.* [10] analyzed nanofluid behavior in the presence of non-identically shaped nanoparticles within a porous medium subjected to the velocity slip effect. Waqas *et al.* [11] analyzed the combined effects of thermal radiation and an exponential heat source on the flow of a 3-D pseudoplastic nanofluid over a Riga surface. Acharya *et al.* [12] explored the behavior and thermal changes in unsteady radiative nanofluid flow around a spinning magnetized disk, employing a Runge–Kutta–Fehlberg numerical scheme. Ma *et al.* [13] numerically examined laminar nanofluid flow and convective heat transfer within microtubes, utilizing a multiphase Eulerian-Lagrangian approach. Bhatti *et al.* [14] focused on the influence of a magnetic dipole on nanofluids flowing over a stretching surface, investigating the impact of variable viscosity and thermal conductivity.

Magnetohydrodynamics (MHDs) delves into the fascinating world of how fluids behave under the influence of external magnetic fields [15]. Introduced by Swedish physicist Alfvén, this branch of mechanics has found diverse applications in engineering, impacting fields like the petroleum industry, power generation, and even crystal formation [15]. Researchers have explored a wide range of MHD applications in fluid flow analysis. Attia investigated heat transfer in dusty fluids subjected to MHD, revealing intriguing temperature fluctuations in both the fluid and particles [16]. Mbeledogu and Ogulu studied the impact of MHD on rotating fluid flow through porous materials, considering the effects of radiation and heat transfer. Their findings highlighted modifications in the boundary layer structure, influencing fluid flow direction [17]. Beyond research, MHD plays a pivotal role in industrial processes like material production and metal casting. Chauhan and Agrawal analyzed MHD flow and heat transfer, uncovering that variables like magnetic field strength and suction rate govern the cooling process [18]. Zheng *et al.* explored heat transfer in 2-D MHD fluid flow on a permeable surface, observing an increase in the thermal boundary layer with adjustments to the system's shrinking parameter [19]. Yazdi *et al.* further demonstrated MHD's potential by studying nanofluid flow, a promising application in various industries [20]. The core of MHD lies in the intricate interaction between the equations governing fluid dynamics and those describing electromagnetism. When a conducting fluid encounters an external magnetic field, an electric current arises, generating a force that interacts with the flow and modifies the magnetic field itself. This complex interplay makes MHD invaluable for understanding and manipulating diverse flow phenomena across various scientific and engineering disciplines [15]. Recent studies by Mirzaei *et al.* and Sagheer *et al.* exemplify the continued exploration of MHD's potential [21, 22]. By investigating heat and mass transfer in complex systems and studying intricate fluid properties, these researchers contribute to our expanding knowledge of MHD and its diverse applications. This ongoing exploration promises to unlock further advancements in numerous fields, solidifying MHD as a powerful tool for the future.

Heat transfer, driven by the temperature differences between objects or within a single object, underpins various technological, and industrial applications like cooling atomic reactors, power generation, and overall energy production. Fourier's Law [23] has been the cornerstone for analyzing heat transfer, but limitations led Cattaneo [24] to introduce a relaxation time term addressing the paradox of instantaneous heat conduction. Christov [25] further refined this theory by incorporating the Oldroyd upper-convected derivative, resulting in the Cattaneo–Christov heat flux theory [25]. Computational methods play a crucial role in studying complex heat transfer scenarios. Recent research exemplifies this trend. Chen *et al.* [26] employed the shooting method

with a Maxwell fluid model to demonstrate that an induced magnetic field can lead to lower temperatures and concentrations at a stagnation point. Lone *et al.* [27] investigated the combined effects of thermal radiation, Joule heating, and Cattaneo–Christov double diffusion on a Casson fluid flow over a stretching surface using the homotopy analysis method within the Buongiorno model framework. Chandan *et al.* [28] analyzed double diffusion convection in a Williamson fluid model considering the influence of a porous medium, utilizing the bvp4c function. Thabet *et al.* [29] explored the influence of Hall current and ion slip within a double-diffusive convective model using the Lobatto IIIA technique.

Entropy, the system's inability to fully utilize available energy, results from factors like heat transfer irreversibility, fluid friction, and mass transfer irreversibility. This cumulative entropy is the sum of these elements, emphasizing the significance of irreversible processes within a system. The increase in entropy over time, dictated by the second law of thermodynamics, is irreversible, particularly in systems involving fluid viscous force, flow-driven force, Joule heating, and thermal management, where heat transfer is inherently irreversible. The scientific and technical communities increasingly recognize entropy generation's importance. Past analyses using various fluid models where aimed to reduce entropy generation in specific systems. Scholars have conducted numerical investigations into entropy generation in convective heat transfer scenarios. Abu-Hijleh *et al.* [30] explored the numerical prediction of entropy generation due to natural convection, while Abu-Nada [31] employed a finite volume approach to study entropy generation arising from reattachment, recirculation, separation, and heat transfer. It was observed that the total entropy generation number increased with increasing Reynolds number. Chen *et al.* [32] utilized the Lattice Boltzmann method to solve the reacting flow model, highlighting that low Reynolds number conditions lead to entropy formation due to the irreversibility of chemical reactions. Non-Newtonian fluid models play a crucial role in simulating the behavior of nanofluids. Ellahi *et al.* [33] applied the Brinkman nanofluid model using the optimal homotopy analysis method. Their findings revealed that the velocity of a shear-thinning fluid decreases with increasing particle volume concentration and size. Hussain *et al.* [34] adopted the Galerkin finite element approach to examine entropy generation resulting from flow induced by upper wall movement and buoyancy forces. Afridi and Qasim [35] observed that the Bejan number decreases with increasing thermal radiation parameter in the boundary layer flow over a thin needle moving in a parallel stream, using a numerical shooting technique. Nayak *et al.* [36] conducted numerical computations using the bvp4c algorithm to study entropy production in the Cattaneo–Christov double diffusion model over a stretched cylinder. Khan *et al.* [37] explored that the Bejan number decays for higher estimations of Weissenberg number in a tangent hyperbolic nanomaterial flow by adopting the homotopy method. More recently, Hussain *et al.* [38] investigated entropy generation in the natural convection of Casson fluid within a porous medium, employing a higher-order Galerkin finite element method. Tanveer *et al.* [39] highlight the significance of analyzing entropy generation to grasp irreversibility in heat transfer. However, the exploration of the specific effects of temperature-dependent viscosity on curved surfaces, especially in the presence of convective conditions.

This research article aims to delve into the intricacies of entropy generation in Catteno–Christov double diffusion MHD Darcy–Forchheimer Williamson fluid flow over a stretchable surface. The primary objective is to enhance system efficiency by minimizing entropy generation, considering influential factors, such as effective Prandtl number, heat generation, thermal radiation, and the Weissenberg number. The study specifically focuses on elucidating the impact of temperature difference and concentration difference on entropy generation. Flow dynamics are induced by a stretching surface, and an orthogonal magnetic field further complicates the system. Numerical solutions are obtained through the shooting technique and Range–Kutta method. The concluding section discusses results, with a particular emphasis on how variations in

temperature and concentration differentials contribute to entropy generation, providing valuable insights for optimizing system performance.

2. Mathematical analysis

The behavior of the Cattaneo–Christov double diffusion model for non-Darcian MHD Williamson nanofluid on the rate of entropy production has been investigated using a stratified sheet. The generation of entropy is examined using the impact of thermal conductivity, Joule dissipation, and the Ohmic effects. The sheet is expected to be stretching in the direction of the x-axis with a velocity $u = U_w(x) = bx$, where b is a positive constant. The physical flow model is shown in Figure 1, where the y-axis is taken perpendicular to the stretching velocity and the x-axis is taken toward the stretching velocity. The ambient temperature is represented by $T_\infty = T_0 + Bx$, and the ambient concentration is represented by $C_\infty = C_0 + Ex$. Temperature andoconcentration at the wall are denotedoby $T_w = T_0 + Ax$ and $C_w = C_0 + Dx$, respectively. With these norms, the governing equations of proposed model are [40]:

$$u_x + v_y = 0, \tag{1}$$

$$uu_x + vu_y = \nu u_{xx} + \sqrt{2}\nu\gamma u_y u_{yy} - \frac{\sigma}{\rho}B_0^2 u - \frac{\nu}{k^*}u - \frac{C_F}{\sqrt{k*}}u^2, \tag{2}$$

$$\begin{aligned}(\rho C_p)_f\left(uT_x + vT_y\right) + \lambda_1\left[(uu_x + vu_y)T_x + (uv_x + vv_y) + u^2T_{xx} + v^2T_{yy} + 2uvT_{xy}\right]\\ = k\left(1 + \frac{16\sigma * T_\infty^3}{3k^*K}\right)T_{yy} + (\rho C_p)_s\left[D_B T_y C_y + \frac{D_T}{T_\infty}\left(T_y\right)^2\right]\\ +\sigma B_0^2 u^2 + \mu_0\left(u_y\right)^2 + \mu_0\gamma\left(u_y\right)^3\end{aligned} \tag{3}$$

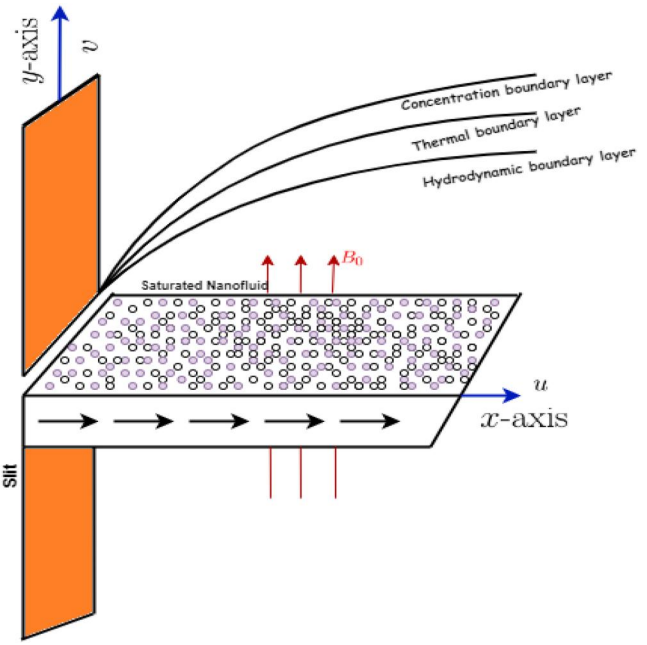

Figure 1. Geometry of physical model.

$$uC_x + vC_y + \lambda_2\left[(uu_x + vu_y)C_x + (uv_x + vv_y)C_y + u^2C_{xx} + v^2C_{yy} + 2uvT_{xy}\right] = D_BC_{yy} + \frac{D_T}{T_\infty}T_{yy} - k_1(C - C_\infty) \tag{4}$$

The associated boundary conditions are as follows [40]:

$$\left.\begin{aligned} y = 0: \quad & u = U_w(x), v = 0, C = C_w, T = T_w, \\ y \to \infty: \quad & u \to 0, T \to T_\infty, C \to C_\infty. \end{aligned}\right\} \tag{5}$$

In the above model, x is the direction around the sheet, the direction perpendicular to the sheet is y, u, and v are the xy-direction horizontal and vertical velocity. Where σ^* is the Stefan–Boltzman constant and k^* is the absorption coefficient. The momentum equation, incorporating term for viscous diffusion (ν), includes additional effects such as magnetic field interaction (σB_0^2), damping (ν/k^*), and nonlinear drag ($C_F/\sqrt{k^*}$). The energy equation governs heat transfer within the fluid, accounting for convective transport, thermal conductivity (K), thermophoresis (D_T), joule heating (σB_0^2), and viscous dissipation (μ_0). Lastly, the concentration equation describes the distribution of a chemical, considering Brownian diffusion (D_B), thermophoretic diffusion (D_T), and chemical reaction constant (k_1).

Non-dimensional similarity variables have been introduced, transforming the above model into a system of nonlinear ODEs, as follows:

$$\left.\begin{aligned} & u = bx\frac{\partial f}{\partial \eta}, v = -(b\nu)^{\frac{1}{2}}f(\eta), \eta = \left(\frac{b}{\nu}\right)^{\frac{1}{2}}y, \\ & \theta(\eta, y) = \frac{T - T_\infty}{T_w - T_\infty}, g(\eta, y) = \frac{C - C_\infty}{C_w - C_\infty}. \end{aligned}\right\} \tag{6}$$

The substitution of Eq. (6) into Eqs. (2)–(4) leads to the derivation of the following system of nonlinear ODEs:

$$\frac{\partial^3 f}{\partial \eta^3} - \left(\frac{\partial f}{\partial \eta}\right)^2 + \frac{\partial f}{\partial \eta}\frac{\partial^2 f}{\partial \eta^2} + We\frac{\partial^2 f}{\partial \eta^2}\frac{\partial^3 f}{\partial \eta^3} - M\frac{\partial f}{\partial \eta} - \lambda\frac{\partial f}{\partial \eta} - Fr\left(\frac{\partial f}{\partial \eta}\right)^2 = 0, \tag{7}$$

$$\left[1 - \lambda_t\left(\frac{\partial f}{\partial \eta}\right)^2 + \frac{4}{3}Rd\left(1 + B_1^3\theta^3 + 3B_1^2\theta^2 + 3B_1\theta\right)\right]\frac{\partial^2 \theta}{\partial \eta^2} - \lambda_t\left(N_2\left(\frac{\partial f}{\partial \eta}\right)^2 - f\frac{\partial^2 f}{\partial \eta^2} + \left(\frac{\partial f}{\partial \eta}\right)^2\theta - f\frac{\partial^2 f}{\partial \eta^2}\theta - f\frac{\partial f}{\partial \eta}\frac{\partial \theta}{\partial \eta}\right) + Pr\left[f\frac{\partial \theta}{\partial \eta} - N_2\frac{\partial f}{\partial \eta} - \frac{\partial f}{\partial \eta}\theta + Nb\left(\frac{\partial \theta}{\partial \eta}\frac{\partial g}{\partial \eta} + \frac{Nt}{Nb}\left(\frac{\partial \theta}{\partial \eta}\right)^2\right) + MEc\left(\frac{\partial f}{\partial \eta}\right)^2 + Ec\left(\frac{\partial^2 f}{\partial \eta^2}\right)^2 + \frac{WeEc}{\sqrt{2}}\left(\frac{\partial^2 f}{\partial \eta^2}\right)^3\right] + \frac{4}{3}Rd\left(3B_1^2\theta^2\left(\frac{\partial \theta}{\partial \eta}\right)^2 + 3B_1\left(\frac{\partial \theta}{\partial \eta}\right)^2 + 6B_1^2\theta\left(\frac{\partial \theta}{\partial \eta}\right)^2\right) = 0, \tag{8}$$

$$\left(1 - \lambda_d f^2\right)\frac{\partial^2 g}{\partial \eta^2} - LePr\left(g\frac{\partial f}{\partial \eta} + N_1\frac{\partial f}{\partial \eta} + f\frac{\partial g}{\partial \eta} + kg\right) + \frac{Nt}{Nb}\frac{\partial^2 \theta}{\partial \eta^2} - \lambda_d\left(N_1\left(\frac{\partial f}{\partial \eta}\right)^2 - N_1 f\frac{\partial^f}{\partial \eta^2} + g\left(\frac{\partial f}{\partial \eta}\right)^2 - 3f\frac{\partial f}{\partial \eta}\frac{\partial g}{\partial \eta}\right) = 0. \tag{9}$$

Under the similarity transformation, the original boundary conditions take the following form:

$$\left.\begin{aligned} &f = 0, \frac{\partial f}{\partial \eta} = 1, g = 1 - N_1, \theta = 1 - N_2 \ \ at \ \ \eta = 0, \\ &\frac{\partial f}{\partial \eta} \to 0, g \to 0, \theta \to 0 \ \ as \ \ \eta \to \infty. \end{aligned}\right\} \tag{10}$$

To analyze the problem, the following non-dimensional quantities are introduced:

$$\left.\begin{aligned} &Pr = \frac{\nu(\rho C_P)_f}{k}, Ec = \frac{b^2x^2}{C_P(Ax)}, We = \sqrt{\frac{2b^3}{\nu}}\gamma x, \\ &M = \frac{\sigma B_0^2}{\rho b}, N_2 = \frac{B}{A}, Nt = \frac{(\rho C_P)_S D_T(T_w - T_0)}{\nu(\rho C_P)_f T_\infty}, \\ &Nb = \frac{(\rho C_P)_S D_B(C_w - C_0)}{\nu(\rho C_P)_f}, \lambda_d = \frac{b\nu\lambda_2}{D_B}, \lambda_t = \frac{\nu b\lambda_1}{k}. \\ &Le = \frac{\alpha}{D_B}, N_1 = \frac{E}{D}, \lambda = \frac{\nu}{\alpha k^*}, Rd = \frac{4\sigma^* T_\infty^3}{k^* K}, \\ &Fr = \frac{xC_F}{\sqrt{k^*}}, N_3 = \frac{T_0}{Bx}, \lambda_t = \frac{\nu a\lambda_1}{k}, B_1 = \frac{1}{N_2(N_3 + 1)}. \end{aligned}\right\} \tag{11}$$

3. Solution framework

The numerical solutions are computed using the shooting method as described through the flowchart in Figure 2, which involves the utilization of the Runge–Kutta technique. A crucial aspect of this method is establishing a suitable finite value far-field boundary condition. This condition

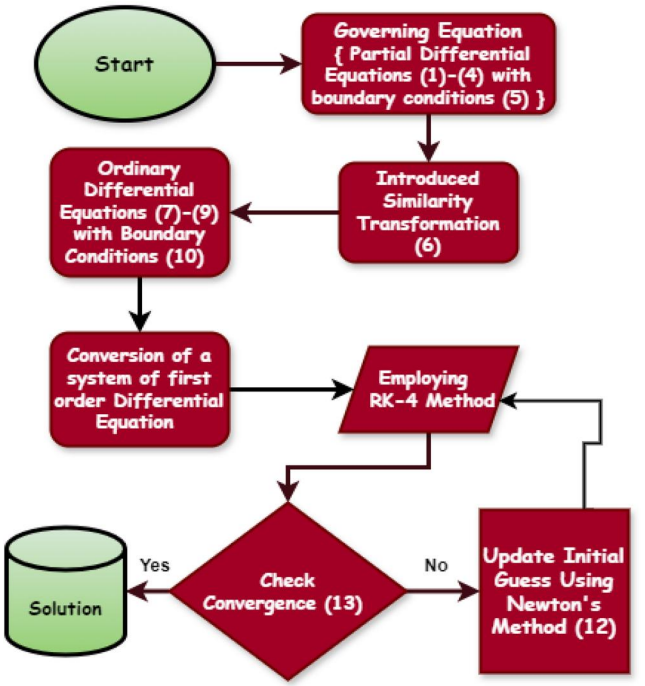

Figure 2. Flowchart of shooting method.

is denoted as $\eta \to \infty$ and specified as $\eta_\infty = 8$ In order to solve the system of ODEs (7)–(9), the following notations have been considered, as an initial step:

$$f = V_1, f' = V_2, f'' = V_3, \theta = V_4, \theta' = V_5, g = V_6, g' = V_7.$$

$$\begin{aligned}
V_1' &= V_2,\\
V_2' &= V_3,\\
V_3' &= \frac{1}{1+WeV_3}\left(V_2^2 - V_1V_3 + MV_2 + \lambda V_2 + FrV_2^2\right)\\
V_4' &= V_5,\\
V_5' &= \frac{1}{1-\lambda_d V_1^2 + \frac{4}{3}Rd\left(1+B_1^3V_4^3+3B_1^2V_4^2+3B_1V_4\right)}\left\{\lambda_t N_2V_2^2 - \lambda_t N_2V_1V_3^2 + \lambda_t V_2^2V_4\right.\\
&\quad -\lambda_t V_1V_3V_4 - \lambda_t V_1V_2V_5 - Pr\left[V_1V_5 - N_2V_2 - V_2V_4 + Nb\left(V_5V_7 + \frac{Nt}{Nb}V_7^2\right) + MEcV_2^2\right.\\
&\quad \left.\left.+EcV_3^2 + \frac{WeEc}{\sqrt{2}}V_3^3\right] - \frac{4}{3}Rd\left[3B_1^2V_4^2V_5^2 + 3B_1V_5^2 + 6B_1^2V_4V_5^2\right]\right\},\\
V_6' &= V_7,\\
V_7' &= \frac{1}{1-\lambda_d V_1^2}\left[LePr(V_2V_6 + N_1V_2 + V_1V_7 + KV_6) - \frac{Nt}{Nb}V_5' + \lambda_d N_1V_2^2 - \lambda_d N_1V_1V_3^2\right.\\
&\quad \left.+\lambda_d V_2^2V_6 - 3\lambda_d V_1V_2V_7\right]
\end{aligned}$$

Initial conditions:

$$\begin{aligned}
&V_1 = 0, V_2 = 1, V_3 = d_1, V_4 = 1 - N_2,\\
&V_5 = d_2, V_6 = 1 - N_1, V_7 = d_3.
\end{aligned}$$

Upon setting the initial values for d_1, d_2, and d_3, the problem is resolved using the shooting technique. To enhance the accuracy of these initial conditions, the Newton method is iteratively applied according to the following scheme:

$$\begin{bmatrix} d_1\\ d_2\\ d_3\end{bmatrix}^{(n+1)} = \begin{bmatrix} d_1\\ d_2\\ d_3\end{bmatrix}^{(n)} - \left(\begin{bmatrix} \frac{\partial V_2}{\partial d_1} & \frac{\partial V_2}{\partial d_2} & \frac{\partial V_2}{\partial d_3}\\ \frac{\partial V_4}{\partial d_1} & \frac{\partial V_4}{\partial d_2} & \frac{\partial V_4}{\partial d_3}\\ \frac{\partial V_6}{\partial d_1} & \frac{\partial V_6}{\partial d_2} & \frac{\partial V_6}{\partial d_3}\end{bmatrix}^{-1}\begin{bmatrix} V_2\\ V_4\\ V_6\end{bmatrix}\right)^{(n)}. \tag{12}$$

This iterative process continues until the satisfaction of the predefined criterion:

$$\max\left\{|V_2(\eta_\infty, d_1, d_2, d_3)|, |V_5(\eta_\infty, d_1, d_2, d_3)|, |V_7(\eta_\infty, d_1, d_2, d_3)|\right\} < 10^{-5}. \tag{13}$$

Furthermore, the validation of the numerical approach is established by comparing the values of skin friction coefficient reported by Khan *et al.* [37] with those computed by the present code, as shown in Table 1.

Table 1. Results of $C_f(Re_x)^{\frac{1}{2}}$ for various parameters.

We	M	Khan *et al.* [37]	Present result
0.1	0.1	2.05608	2.05613
0.2		2.01101	2.01106
0.3		1.96124	1.96135
	0.2	2.14587	2.14589
	0.3	2.23184	2.23185

4. Physical quantities of interest

The physical parameters, including the skin friction, Nusselt number, and Sherwood number, are defined by as:

$$C_{fx} = \frac{-2(\tau_w)_{y=0}}{\rho u_w^2(x)}, \quad Nu_x = \frac{xq_w}{k(T_w - T_\infty)} \quad Sh_x = \frac{xq_m}{D_B(C_w - C_\infty)}. \tag{14}$$

Here, τ_w denotes the shear stress, q_w signifies the wall heat flux, and q_m represents the concentration flux from the surface. These parameters are mathematically expressed as:

$$\tau_w = \mu\left[\frac{\partial v_1}{\partial y} + \frac{\gamma}{\sqrt{2}}\left(\frac{\partial v_1}{\partial y}\right)^2\right]_{y=0}, q_w = -\left(k + \frac{16T_\infty^3\sigma^*}{3k^*}\right)(Ax\left(\frac{b}{\nu}\right)^{1/2}\theta'(\eta))_{\eta=0},$$

$$q_m = -D_B(Dx\left(\frac{b}{\nu}\right)^{1/2}g'(\eta))_{\eta=0}.$$

By substituting Eq. (6) into Eq. (14) and simplifying each term, we derive the dimensionless parameters in the following form:

$$C_{fx}(Re_x)^{\frac{1}{2}} = -\left[2f''(0) + Wef''^2(0)\right], Sh_x(Re_x)^{-\frac{1}{2}} = \frac{-g'(0)}{(1 - N_1)},$$

$$Nu_x(Re_x)^{-\frac{1}{2}} = \frac{\theta'(0) + \frac{4}{3}Rd\ \theta'(0)}{(N_2 - 1)}.$$

5. Entropy generation

The rate of entropy generation E_G for Cattaneo–Christov double diffusion model has been discussed briefly in Chu *et al.* [41]. The dimensional form of E_G is given below.

$$E_G = \underbrace{\frac{1}{T_\infty^2}\left[K(T_y)^2 + \frac{16\sigma^*T^3}{3KK^*}K(T_y)^2\right]}_{\text{Heat Transfer Irreversibility}} + \underbrace{\frac{RD_B}{C_\infty}(C_y)^2}_{\text{Mass Transfer Irreversibility}} + \underbrace{\frac{\sigma}{T_\infty}B_0^2u^2\frac{RD_w}{C_\infty}C_yT_y}_{\text{Joul Heating Irreversibility}}$$

$$+ \underbrace{\frac{1}{T_\infty}\left[\mu_0(u_y)^2 + \mu_0\gamma(u_y)^3 + \alpha_1(uu_yu_{xy} + vu_yu_{yy}) + 2\alpha_2(u_y)^4\right]}_{\text{Fluid Friction Irreversibility}}. \tag{15}$$

By using similarity transformation (6), we can achieve the dimensionless form of entropy generation as:

$$N_G = \frac{T_\infty \nu}{k(T_w - T_0)\alpha} = \tau_1 \left[1 + \frac{4}{3} Rd \left(\frac{\theta}{N_2(N_3+1)}\right)^3\right]\theta^2 + L\frac{\tau_2}{\tau_1}\left(\frac{\partial g}{\partial \eta}\right)^2 + L\frac{\partial \theta}{\partial \eta}\frac{\partial g}{\partial \eta} + Br\left(\frac{\partial^2 f}{\partial \eta^2}\right)^2 + MBr\left(\frac{\partial f}{\partial \eta}\right)^2 + X_b\left(\frac{\partial^2 f}{\partial \eta^2}\right)^4 \frac{WeBr}{\sqrt{2}}\left(\frac{\partial^2 f}{\partial \eta^2}\right)^3 + X_r\left(\frac{\partial f}{\partial \eta}\left(\frac{\partial^2 f}{\partial \eta^2}\right)^2 - f\frac{\partial^2 f}{\partial \eta^2}\frac{\partial^3 f}{\partial \eta^3}\right), \tag{16}$$

where $Br = \frac{b^2\mu_0 x^2}{k(T_w - T_0)}$ denotes the Brinkman number, $\tau_1 = \frac{T_w - T_0}{T_\infty}$ is dimensionless temperature gradient, $L = \frac{RD_A(C_w - C_0)}{k}$ represents the diffusion parameter, $Xr = \frac{b^3 x^2 \alpha_1}{K(T_w - T_0)}$ and $X_b = \frac{2b^2 x^4 \alpha^2}{K(T_w - T_0)\nu}$ are Cattaneo-Christov double diffusion entropy parameters and $\tau_2 = \frac{C_w - C_0}{C_\infty}$ is the non-dimensional concentration difference parameter.

Table 2. Results of $C_f(Re_x)^{\frac{1}{2}}$ for various parameters.

M	We	λ	Fr	$C_f(Re_x)^{\frac{1}{2}}$	I_f	DC_f
0.3	0.3	0.2	0.1	2.30701	[−1,4]	
0.5				2.43594	[0,4]	5.6
0.7				2.55552	[−1,5]	4.9
0.9				2.66702	[−1,6]	4.4
	0.35			2.26569	[−1,6]	1.8
	0.40			2.21929	[0,5]	2.0
	0.45			2.16399	[−1,7]	2.5
		0.3		2.37274	[−1,4]	2.4
		0.4		2.43594	[−1,4]	2.7
		0.5		2.49681	[−1,4]	2.5
			0.2	2.34984	[−1,5]	1.8
			0.3	2.39166	[−1,4]	1.8
			0.4	2.43251	[−2,4]	1.7

Table 3. Results of $Nu(Re_x)^{-\frac{1}{2}}$ and $Sh(Re_x)^{-\frac{1}{2}}$ when $N_1 = 0.8$, $N_2 = 0.8$, $N_3 = 1.0$, $Pr = 0.7$, $Le = 1.0$, and $We = 0.3$.

k	M	λ_t	λ_d	Rd	N_t	$Nu(Re_x)^{-\frac{1}{2}}$	$Sh(Re_x)^{-\frac{1}{2}}$	I_θ	I_g	DNu	DSh
0.1	0.3	0.1	0.1	0.3	0.5	1.70985	1.74825	[−0.5, 0.2]	[−0.5, 0.3]	–	–
0.2						1.70945	1.77680	[−0.3, 0.1]	[−0.4, 0.1]	0.02	1.6
0.3						1.70904	1.80501	[−0.4, 0.1]	[−0.3, 0.2]	0.02	1.6
0.4						1.70865	1.83263	[−0.4, 0.1]	[−0.5, 0.2]	0.02	1.5
	0.4					1.60433	1.75192	[−0.5, 0.2]	[−0.5, 0.3]	6.2	0.2
	0.5					1.50437	1.75673	[−0.5, 0.2]	[−0.5, 0.3]	6.2	0.3
	0.6					1.40946	1.76246	[−0.5, 0.1]	[−0.4, 0.3]	6.3	0.3
		0.98				3.89998	0.51412	[−0.4, −0.1]	[−0.4, −0.1]	128.1	70.6
		0.96				3.85151	0.54140	[−0.5, −0.1]	[−0.5, −0.2]	1.2	5.3
		0.94				3.80296	0.56872	[−0.5, −0.1]	[−0.5, −0.1]	1.3	5.0
			0.98			1.66548	4.04724	[−0.4, 0.1]	[−0.4, 0.2]	2.6	131.5
			0.96			1.66638	3.99659	[−0.4, 0.1]	[−0.4, 0.3]	0.1	1.3
			0.94			1.66727	3.94585	[−0.4, 0.2]	[−0.4, 0.2]	0.05	1.3
				0.4		0.21654	0.36098	[−0.5, 0.2]	[−0.4, 0.3]	87.3	79.4
				0.5		0.20227	0.37353	[−0.5, 0.2]	[−0.5, 0.3]	6.6	3.5
				0.6		0.19032	0.38401	[−0.5, 0.2]	[−0.4, 0.3]	5.9	2.8
					0.6	1.70587	1.58473	[−0.4, 0.2]	[−0.4, 0.4]	0.2	9.3
					0.7	1.70191	1.42209	[−0.5, 0.1]	[−0.5, 0.2]	0.2	10.3
					0.8	1.69797	1.26035	[−0.3, 0.2]	[−0.4, 0.3]	0.2	11.4

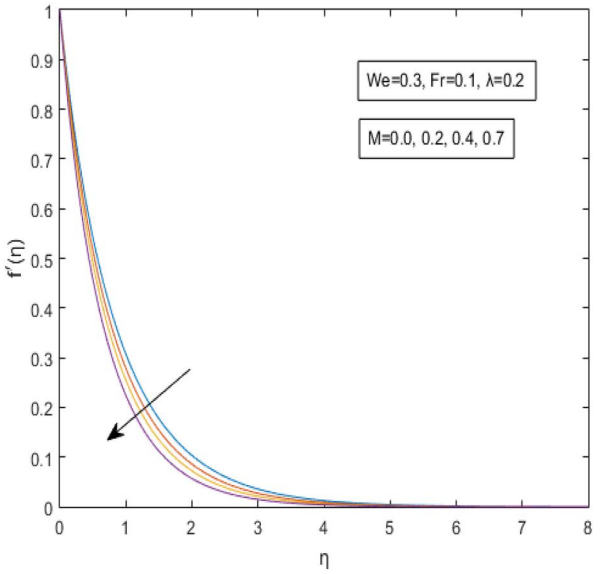

Figure 3. $f'(\eta)$ for different values of *M*.

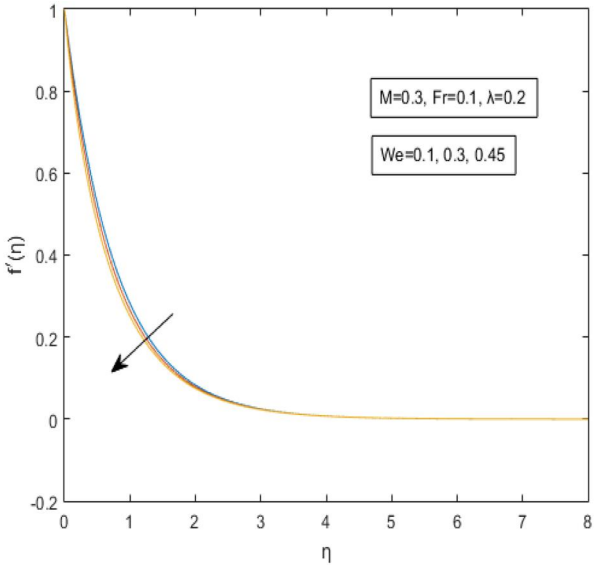

Figure 4. $f'(\eta)$ for increasing value of *We*.

6. Results and discussions

The ongoing segment consists of the discussion related to the numerical solution of the system of ODEs that governs the flow problem in the dimentionless form. With the aid of tables and graphs, the numerical data for the non-Darcian MHD Williamson Nanofluid with Cattaneo–Christov double diffusion model has been presented. This includes the temperature profile $\theta(\eta)$ and concentration profile $g(\eta)$, as well as the previously discussed physical parameters.

Table 2 illustrates the impact of various dimensionless parameters on the skin friction coefficient, denoted as $(Re_x)^{1/2}C_f$. The table indicates that an increase in the magnetic parameter (M), porosity parameter (λ), and inertial coefficient (Fr) results in a increase in the skin friction

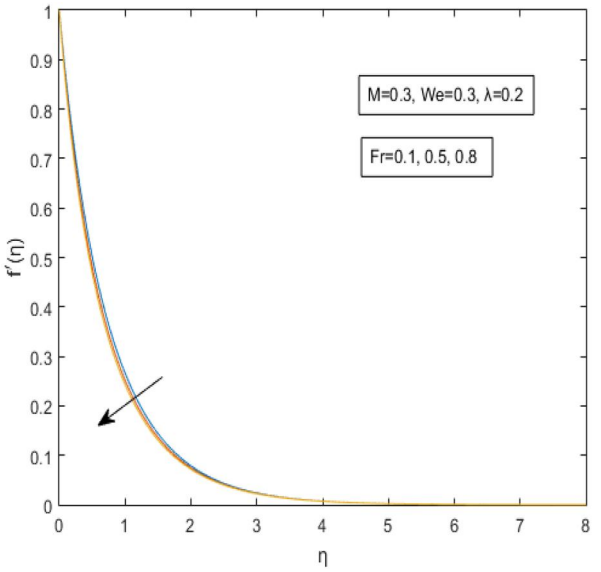

Figure 5. $f'(\eta)$ for different values of *Fr*.

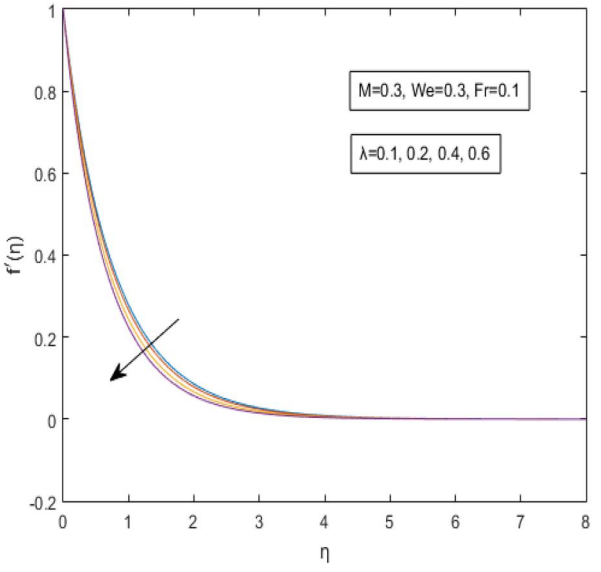

Figure 6. $f'(\eta)$ for various value of λ.

coefficient. Likewise, a rise in the Weissenberg number (We) correlates with a reduction in the skin friction coefficient. Furthermore, Table 2 provides an interval labeled as I_f, which assists in selecting initial guess conditions for the momentum equation, and DC_f shows the absolute percentage change in the skin friction coefficient.

Table 3 examines the influence of various dimensionless parameters on the Nusselt and Sherwood numbers. It presents the values of these numbers corresponding to changes in the chemical reaction parameter, magnetic parameter, Cattaneo–Christov temperature parameter (λ_t), Cattaneo–Christov concentration parameter (λ_d), thermal radiation parameter, and thermophoresis parameter. Intervals labeled as I_θ and I_ϕ are included for selecting missing conditions for the energy and concentration equations, respectively. An increase in the chemical reaction parameter

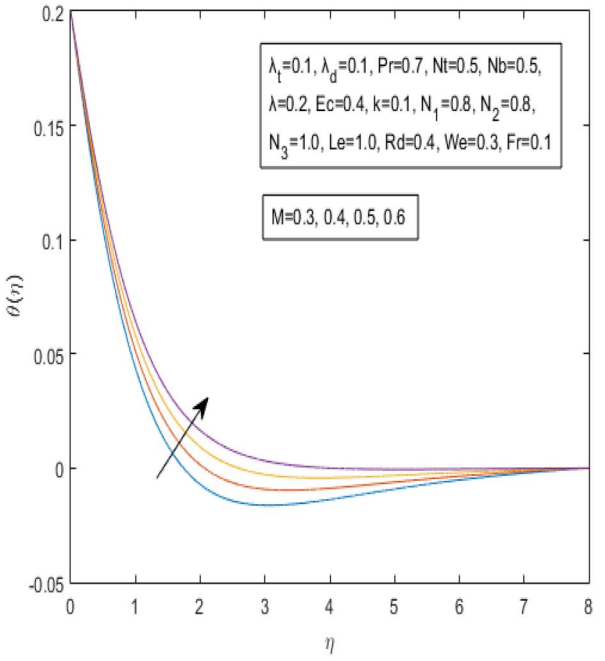

Figure 7. The effect of *M* on $\theta(\eta)$.

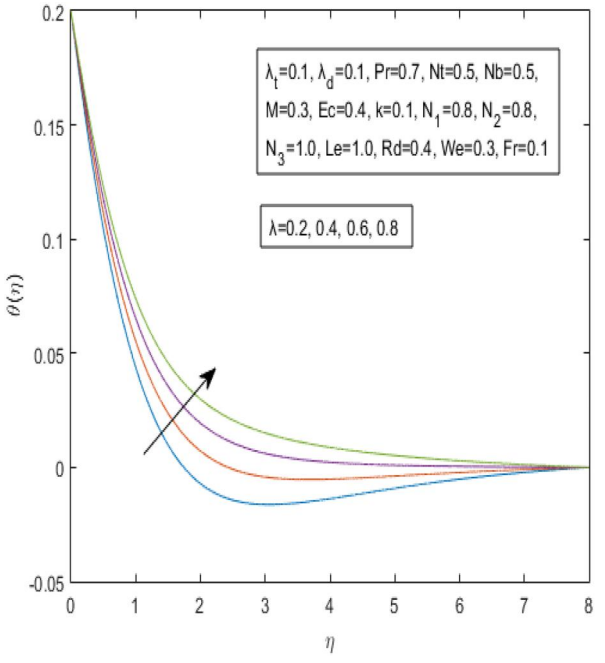

Figure 8. The effect of porosity constant λ on $\theta(\eta)$.

(k) leads to a gradual decrease in the Nusselt number and an increase in the Sherwood number. The Sherwood number exhibits a gradual increase, while the Nusselt number experiences a rapid decrease with an increase in the magnetic parameter. A rise in the Cattaneo–Christov temperature parameter (λ_t) results in an increase in the Nusselt number but a decrease in the Sherwood

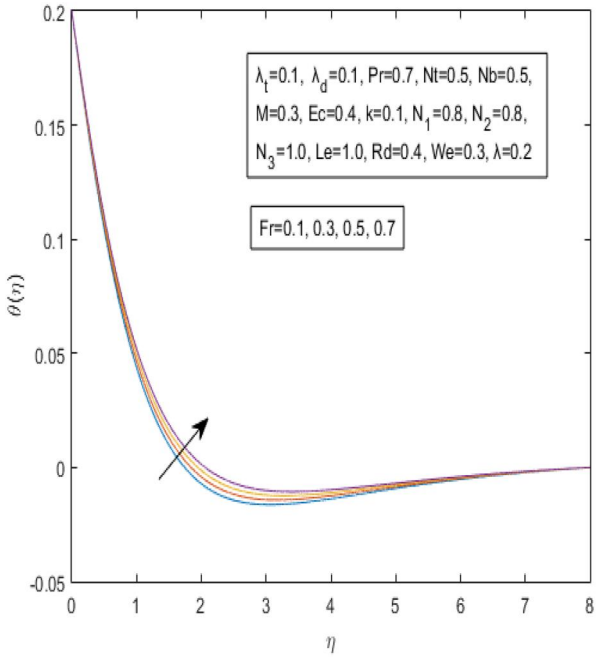

Figure 9. The effect of inertial coefficients *Fr* on $\theta(\eta)$.

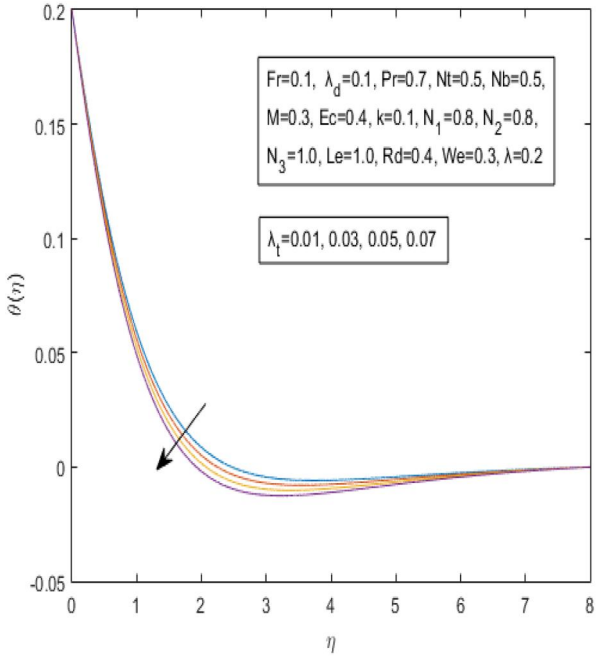

Figure 10. The effect of λ_t on $\theta(\eta)$.

number. Conversely, an increase in the Cattaneo–Christov concentration parameter (λ_d) causes a slow decrease in the Nusselt number and a slight increase in the Sherwood number. Moreover, an increase in the thermal radiation parameter leads to a decrease in the Nusselt number and an increase in the Sherwood number. Finally, an increase in the thermophoresis parameter results in a modest decrease

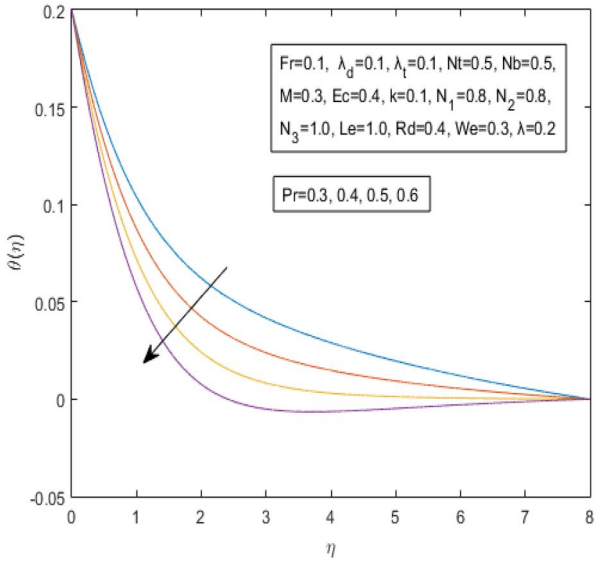

Figure 11. The effect of *Pr* on $\theta(\eta)$.

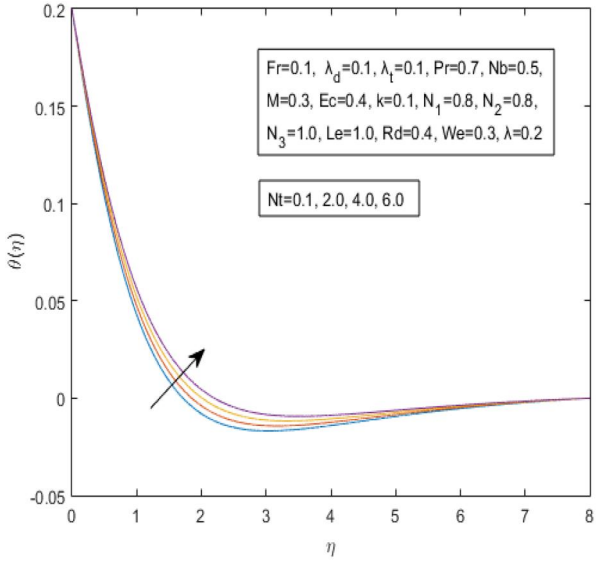

Figure 12. The effect of *Nt* on $\theta(\eta)$.

in the Nusselt number and a significant decrease in the Sherwood number, where *DNu* and *DSh* show the absolute percentage change in the Nusselt and Sherwood numbers, respectively.

6.1. Velocity profile

An increment in the value of the magnetic parameter results a decline in the velocity profile and this phenomenon can be visulized from Figure 3. As the parameter *M* physically induces a resistive force in the conductive fluid that's why in Figure 3, a drop in the fluid velocity is seen as a result of this produced resistive force. Similarly, as the value of Weissenberg number increases, a decline in the velocity profile is notable and this can be seen through Figure 4. The Weissenberg number, which

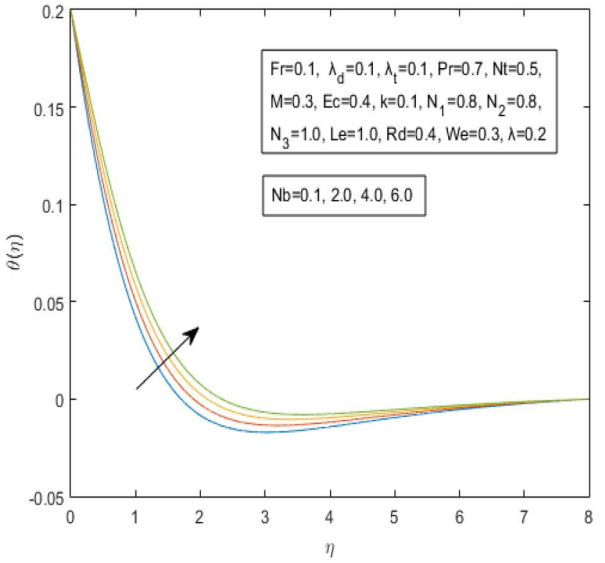

Figure 13. The effect of *Nb* on $\theta(\eta)$.

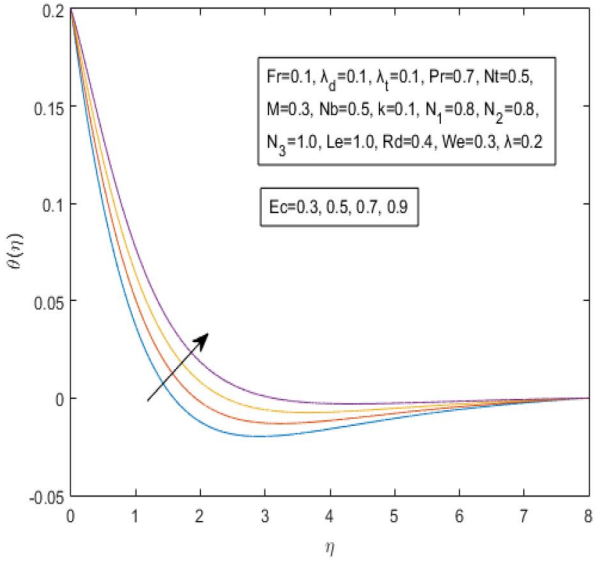

Figure 14. The effect of *Ec* on $\theta(\eta)$.

describes the relationship between the relaxation time and the time scale of fluid flow, states that as *We* increases, the relaxation period lengthens, allowing for greater flow resistance. As a result, the thickness of the associated boundary layer grows, causing the fluid's velocity to decline. Figure 5 depicts that due to an increasing value of the inertial coefficient, the velcoity profile decreases and a similar phenomenon can be seen for the porosity parameter through Figure 6.

6.2. Temperature profile

Here, a thorough discussion on the impact of several dimensionless characteristics on the temperature profile has been conducted. In this comprehensive study, we have thoroughly examined

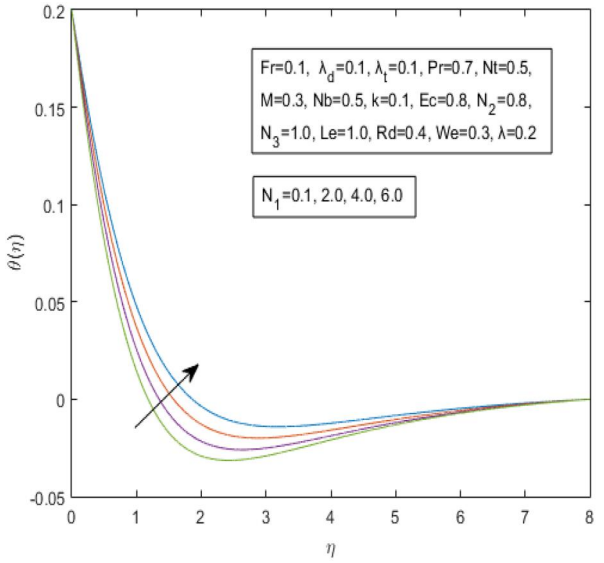

Figure 15. The effect of N_1 on $\theta(\eta)$.

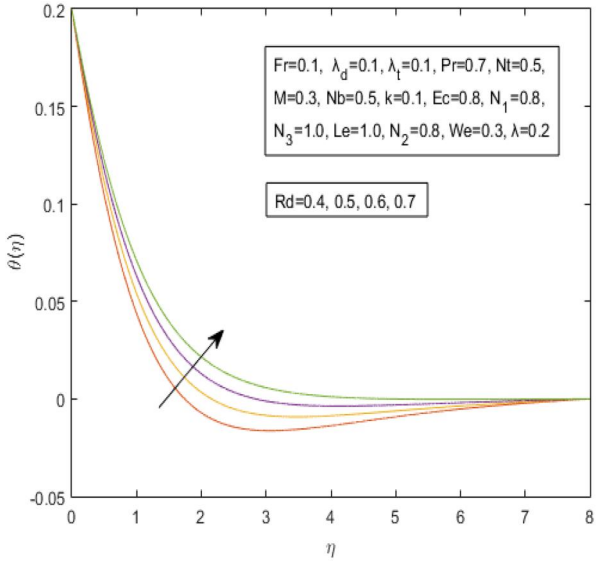

Figure 16. The effect of *Rd* on $\theta(\eta)$.

how various characteristics affect the temperature profile. A small increment in the magnetic number leads to a higher temperature distribution due to a resistive force created in the fluid's flow direction (Figure 7). Additionally, as the porosity parameter increases, indicating more space in the material, the temperature profile also rises (Figure 8). A clear relationship is observed between the temperature profile and the inertial coefficient, with a higher inertial coefficient associated with a larger thermal boundary layer (Figure 9). Conversely, higher values of the Cattaneo–Christov temperature parameter result in a decrement in the temperature profile (Figure 10). Elevating the Prandtl number leads to a lower temperature field, reflecting a reduced rate of heat transmission (Figure 11). Furthermore, the temperature profile shows an increasing trend with a rise in the thermophoresis parameter, where nanoparticles move from hotter to

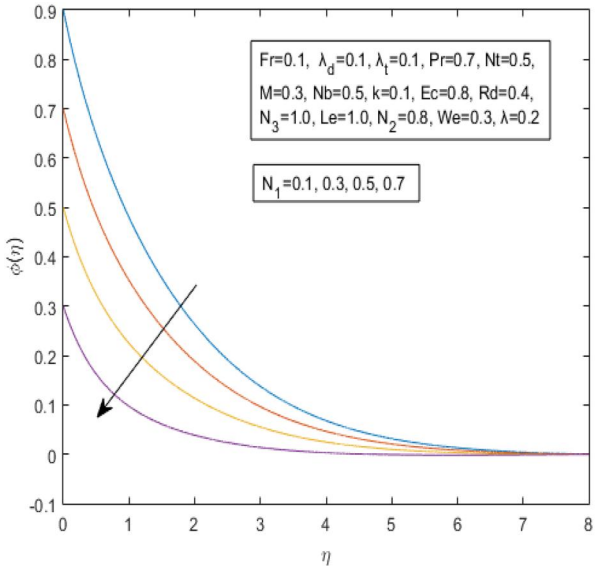

Figure 17. The effect of N_1 on $g(\eta)$.

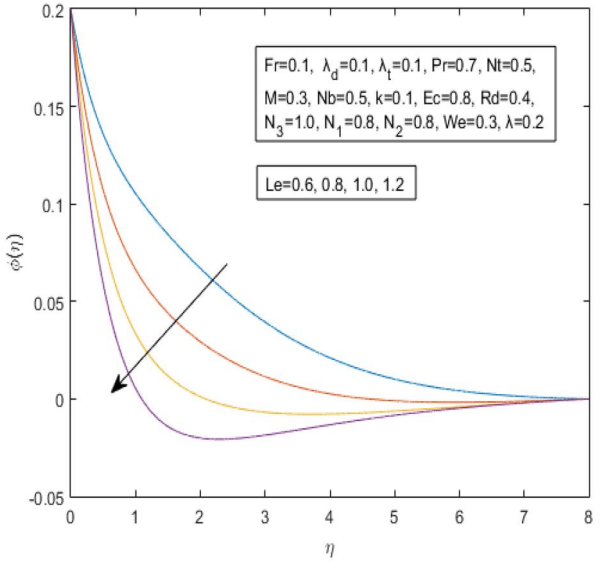

Figure 18. The effect of *Le* on $g(\eta)$.

cooler regions, amplifying the overall temperature distribution (Figure 12). An increment in the Brownian motion parameter corresponds to an escalating temperature profile, because higher Brownian motion intensifies fluid motion and kinetic energy (Figure 13). Moreover, the temperature distribution rises with an increase in the Eckert number, indicating heightened kinetic energy of fluid particles and an expanded thickness of the thermal boundary layer (Figure 14). The solutal stratification parameter N_1 also effect the temperature profile, with an ascending trend depicted in Figure 15. The temperature profile rises concomitantly with the thermal radiation parameter, facilitating enhanced heat delivery to the fluid and increasing the temperature distribution $\theta(\eta)$ (Figure 16).

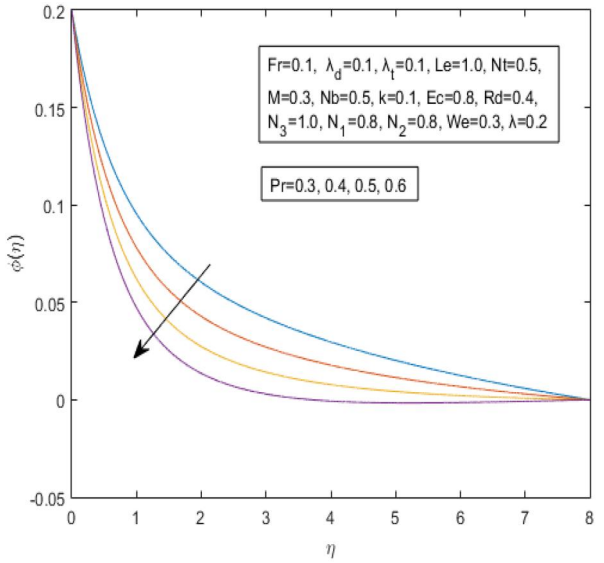

Figure 19. The effect of *Pr* on $g(\eta)$.

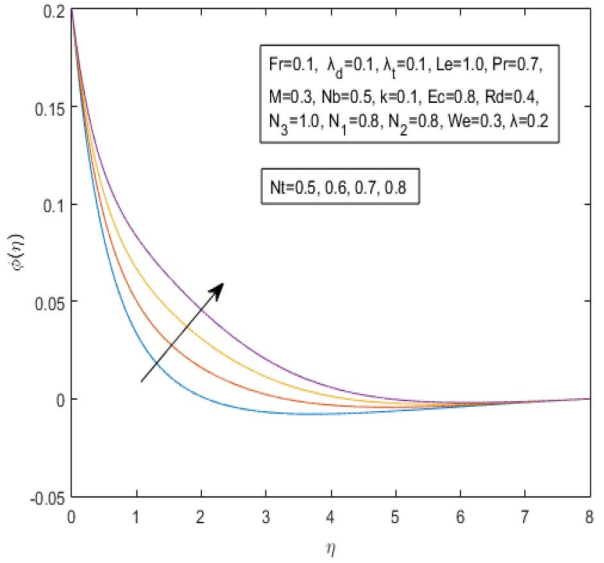

Figure 20. The effect of *Nt* on $g(\eta)$.

6.3. Concentration profile

This section provides a brief overview of the behavior of the concentration profile subjected to a various dimensionless parameters. The concentration profile has been observed to respond to changes in distinct dimensionless parameters as summarized from the plotted graphs.

An upward variation in the solutal stratification parameter corresponds to a downward shift in the concentration profile, as depicted in Figure 17. This behavior highlights the influence of stratification in limiting solute diffusion, creating a more pronounced gradient within the boundary layer. Similarly, the concentration profile increases with the escalation of the Lewis number, as illustrated in Figure 18. The enhanced mass diffusivity relative to thermal diffusivity suggests more efficient solute diffusion compared to heat transfer.

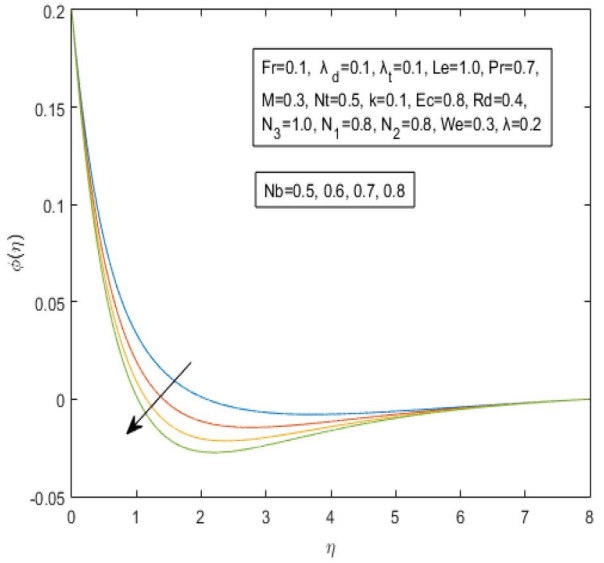

Figure 21. The effect of *Nb* on $g(\eta)$.

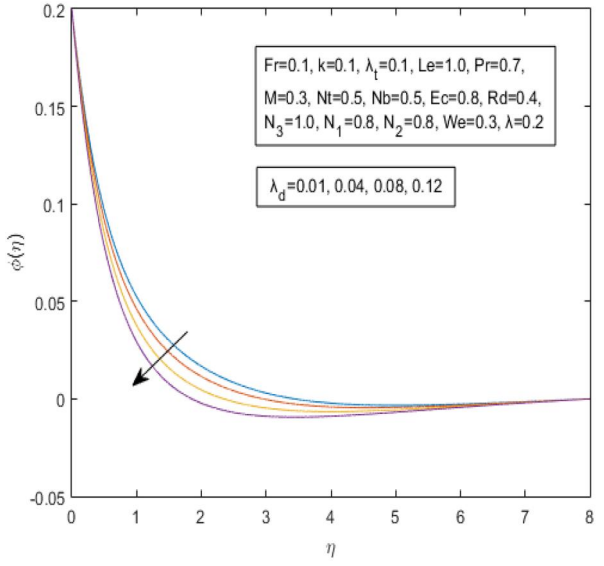

Figure 22. The effect of λ_d on $g(\eta)$.

Elevated Prandtl numbers, on the other hand, lead to a decline in the concentration profile, as seen in Figure 19. Higher Prandtl numbers indicate dominant momentum diffusivity over thermal diffusivity, resulting in a thinner thermal boundary layer and reduced solute concentration. The behavior of the concentration profile responds inversely to the rising values of the thermophoresis parameter, displaying a decreasing pattern in Figure 20. The increase in the thermophoresis parameter, which reflects the movement of particles in response to temperature gradients, suggests a stronger thermophoretic force driving particles away from the hot region, thereby lowering the local solute concentration.

Likewise, an increase in the Brownian motion parameter results in a decrease in the concentration profile, as observed in Figure 21. Brownian motion, indicative of particle diffusion due to

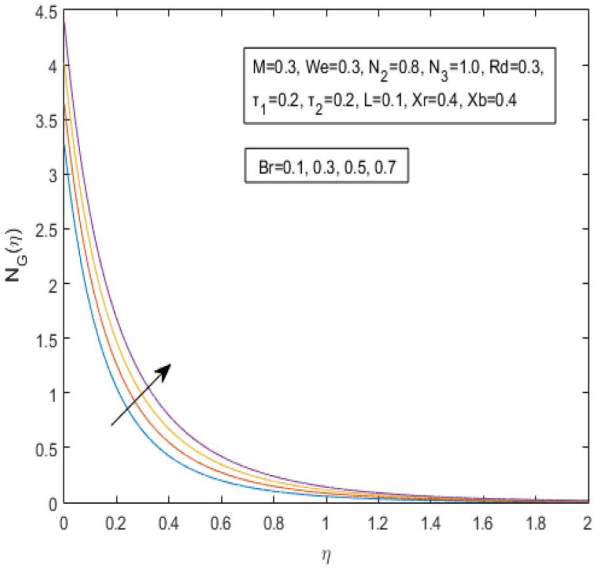

Figure 23. Entropy profile for higher value of *Br*.

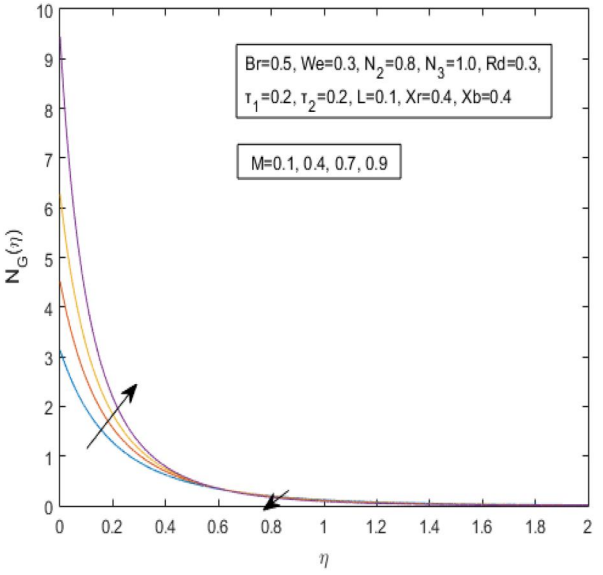

Figure 24. The effect of *M* on N_G.

random thermal fluctuations, enhances mixing and reduces solute concentration gradients. Lastly, a decreasing trend in the concentration distribution is evident with an increment in the Cattaneo–Christov concentration parameter, λ_d, as depicted in Figure 22. This parameter accounts for relaxation time effects in concentration diffusion, and its increase suggests a delay in the diffusion process, resulting in lower solute concentration near the boundary.

6.4. Entropy analysis

This section discusses the impact of various non-dimentional parameters on the entropy generation. The following points illsutrate the implications of different graphs presented in this section.

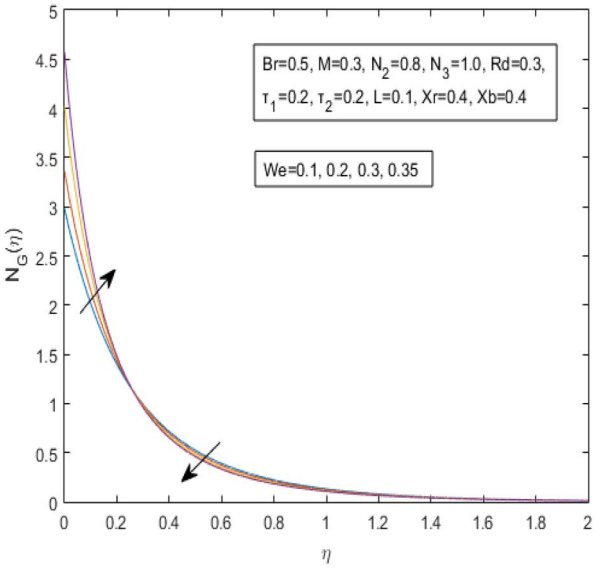

Figure 25. The effect of *We* on N_G.

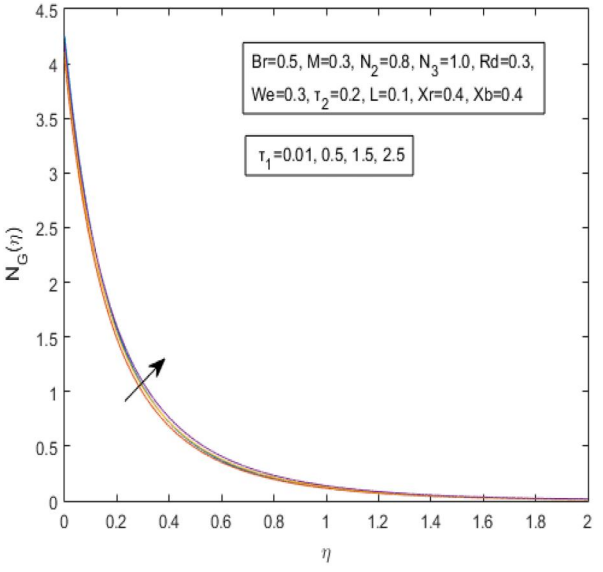

Figure 26. The effect of τ_1 on N_G.

Figure 23 displays the impact of the Brinkman number on entropy generation. The Brinkman number attributes viscous heating to molecular absorption, leading to a reduction in the rate of heat transfer. The accumulation of a significant amount of heat within the layers of the non-Newtonian fluid is the primary contributor to the observed rise in entropy generation, indicating the role of viscous dissipation in enhancing thermal disorder within the fluid. In Figure 24, the gradual effect of the magnetic parameter on entropy generation is depicted. The entropy produced in the system shows a direct correlation with the strength of the magnetic field, particularly away from the surface, with a slightly decreasing pattern observed in proximity to the surface. This suggests that the magnetic field's influence on Lorentz force contributes to increased irreversibilities in the flow system, affecting the entropy generation distribution.

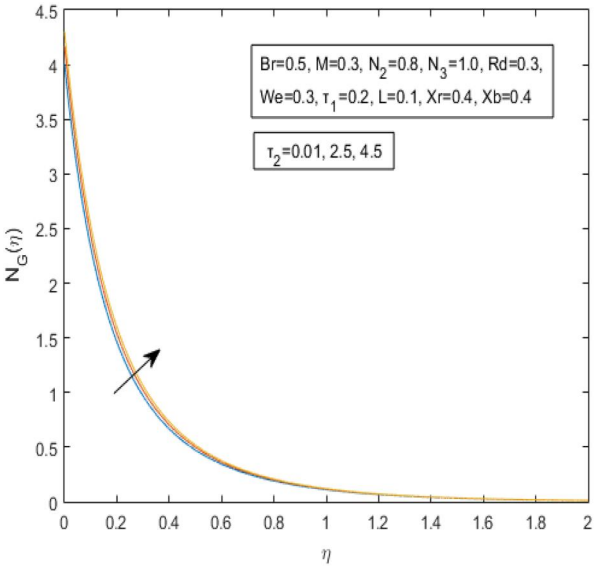

Figure 27. The effect of τ_2 on N_G.

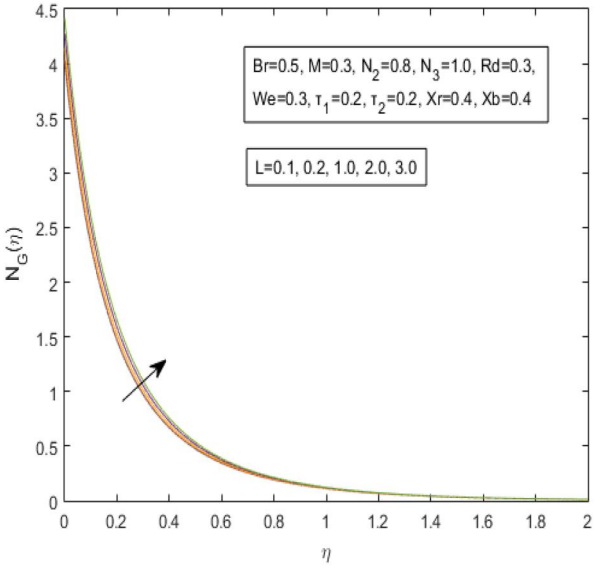

Figure 28. The effect of L on N_G.

The rate of entropy generation with respect to the Weissenberg number *We* is discussed in Figure 25. As the Weissenberg number rises, the entropy generation rate increases away from the surface and then shows a decreasing behavior near the surface. This indicates that elasticity in the fluid, characterized by the Weissenberg number, enhances entropy production due to increased molecular interactions and deformation rates. Furthermore, the entropy generation displays an increasing pattern when the value of the temperature difference parameter increases, as seen through Figures 26 and 27. Higher temperature differences amplify thermal gradients, thereby increasing the rate of heat transfer irreversibility and consequently the entropy generation.

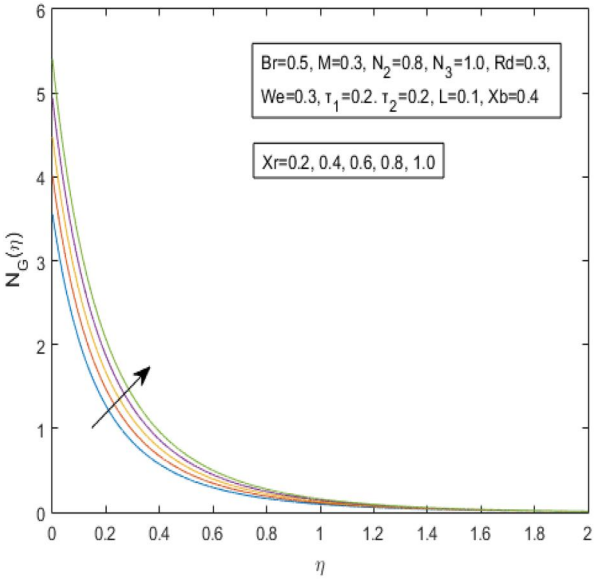

Figure 29. The effect of *Xr* on N_G.

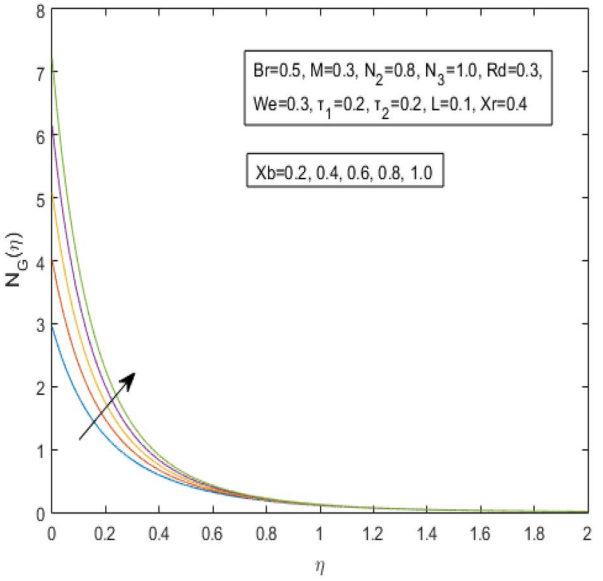

Figure 30. The effect of *Xb* on N_G.

The entropy production also displays an increasing pattern as the diffusion parameter's value increases, as shown in Figure 28. This reflects the effect of mass diffusion processes on entropy generation, where greater diffusion leads to higher mass transfer irreversibilities. Finally, Figures 29 and 30 illustrate the effect of the Cattaneo-Christov double diffusion parameters on entropy generation. The increase in entropy generation with these parameters suggests that the relaxation times for heat and mass fluxes introduce delays in the diffusion processes. This behavior results in greater molecular disorder and irreversibilities in the system, enhancing the overall entropy production.

7. Conclusion

This study examined the entropy generation in Williamson fluid flow over a stretching sheet, incorporating viscous dissipation, inclined magnetic field, and Cattaneo–Christov heat flux effects. Such insights advance understanding beyond previous studies, offering significant implications for diverse applications in solar engineering, polymer extrusion, electronic components, and biomedicine. Numerical results are acquired through the shooting method. The numerical code is validated against existing literature, demonstrating strong agreement. Key physical parameters are elucidated graphically. Our findings highlight:

- The fluid velocity diminishes with elevated values of λ, Fr, and We.
- The temperature profile rises with increasing N_1, Nb, Nt, and Rd, but declines with greater λ_t and Pr.
- The concentration profile reduces with higher Nb, Le, and N_1, but enhances with increasing Nt.
- Due to the ascending values of the relaxation time parameter γ_1, the values of Nu_x are increased while Sh_x is decreased.
- The Brinkman number reduces the heat transfer rate, leading to increased entropy generation within the fluid.
- Entropy generation initially rises with increasing Weissenberg number (We) and magnetic field parameter (M), but decreases near the surface.
- The lowest entropy generation values, N_G, are observed for the magnetic field parameter $M = 0.9$ and for the Weissenberg number $We = 0.35$.

Disclosure statement

No potential conflict of interest was reported by the author(s).

ORCID

M. Sagheer http://orcid.org/0000-0001-5984-4492
S. Hussain http://orcid.org/0000-0003-1023-1534

References

[1] Y. Cengel, J. Cimbala and R. Turner, *Fundamentals of Thermal-Fluid Sciences (SI units)*. New York, NY: McGraw Hill, 2012. DOI: 978–9814720953.
[2] B. Xia and D. W. Sun, "Applications of computational fluid dynamics (cfd) in the food industry: a review," *Comput. Electron. Agric.*, vol. 34, no. 1–3, pp. 5–24, 2002. DOI: 10.1016/S0168-1699(01)00177-6.
[3] E. P. Shipley, *Study of Natural Gas Vehicles (NGV) during the Fast Fill Process*. Morgantown, WV: West Virginia University, 2002. DOI: 10.33915/etd.1264.
[4] R. V. Williamson, "The flow of pseudoplastic materials," *Ind. Eng. Chem.*, vol. 21, no. 11, pp. 1108–1111, 1929. DOI: 10.1021/ie50239a035.
[5] S. Nadeem, S. T. Hussain and C. Lee, "Flow of a Williamson fluid over a stretching sheet," *Braz. J. Chem. Eng.*, vol. 30, no. 3, pp. 619–625, 2013. DOI: 10.1590/S0104-66322013000300019.
[6] S. Shaheen, M.B., Arain, K. S. Nisar, A. Albakri, M. D. Shamshuddin, F. O. Mallawi, and Usman, "A case study of heat transmission in a Williamson fluid flow through a ciliated porous channel: a semi-numerical approach" *Case Stud. Thermal Eng.*, vol. 41, pp. 102523, 2023, DOI: 10.1016/j.csite.2022.102523.
[7] A. M. Obalalu, S. O. Salawu, O. A. Olayemi, O. A. Ajala and K. Issa, "Analysis of hydromagnetic Williamson fluid flow over an inclined stretching sheet with hall current using Galerkin weighted residual method," *Comput. Math. Appl.*, vol. 146, pp. 22–32, 2023. DOI: 10.1016/j.camwa.2023.06.021.
[8] S. U. S. Choi, "Nanofluid technology: current status and future research," Technical Report, Argonne, IL: Argonne National Lab. (ANL), 1998.

[9] J. A. Eastman, S. R. Phillpot, S. U. S. Choi and P. Keblinski, "Thermal transport in nanofluids" *Annu. Rev. Mater. Res.*, vol. 34, no. 1, pp. 219–246, 2004. DOI: 10.1146/annurev.matsci.34.052803.090621.

[10] I. Rashid, M. Sagheer and S. Hussain, "Magnetohydrodnamics nanofluid flow of shaped nanoparticles over a porous stretching wall and slip effect" *Numer. Methods Partial*, vol. 39, no. 2, pp. 866–889, 2023. DOI: 10.1002/num.22780.

[11] H. Waqas *et al.*, "Gyrotactic motile microorganisms impact on pseudoplastic nanofluid flow over a moving riga surface with exponential heat flux," *Crystals*, vol. 12, no. 9, pp. 1308, 2022. DOI: 10.3390/cryst12091308.

[12] N. Acharya, F. Mabood, S. A. Shahzad and I. A. Badruddin, "Hydrothermal variations of radiative nanofluid flow by the influence of nanoparticles diameter and nanolayer," *Int. Commun. Heat Mass Transf.*, vol. 130, pp. 105781, 2022. DOI: 10.1016/j.icheatmasstransfer.2021.105781.

[13] H. Ma, B. He, L. Su and D. He, "Heat transfer enhancement of nanofluid flow at the entry region of microtubes," *Int. J. Thermal Sci.*, vol. 184, pp. 107944, 2023. DOI: 10.1016/j.ijthermalsci.2022.107944.

[14] M. M. Bhatti and R. Ellahi, "Numerical investigation of non-darcian nanofluid flow across a stretchy elastic medium with velocity and thermal slips," *Numer. Heat Transf. B Fundamental.*, vol. 83, no. 5, pp. 323–343, 2023. DOI: 10.1080/10407790.2023.2174624.

[15] H. Alfvén, "Existence of electromagnetic-hydrodynamic waves," *Nature*, vol. 150, no. 3805, pp. 405–406, 1942. DOI: 10.1038/150405d0.

[16] H. A. Attia, "Unsteady MHD Couette flow and heat transfer of dusty fluid with variable physical properties," *Appl. Math. Comput.*, vol. 177, no. 1, pp. 308–318, 2006. DOI: 10.1016/j.amc.2005.11.010.

[17] I. U. Mbeledogu and A. Ogulu, "Heat and mass transfer of an unsteady MHD natural convection flow of a rotating fluid past a vertical porous flat plate in the presence of radiative heat transfer," *Int. J. Heat Mass Transf.*, vol. 50, no. 9–10, pp. 1902–1908, 2007. DOI: 10.1016/j.ijheatmasstransfer.2006.10.016.

[18] D. S. Chauhan and R. Agrawal, "MHD flow and heat transfer in a channel bounded by a shrinking sheet and a plate with a porous substrate" *J. Eng. Phys. Thermophy.*, vol. 84, no. 5, pp. 1034–1046, 2011. DOI: 10.1155/2013/291270.

[19] L. Zheng, J. Niu, X. Zhang and Y. Gao, "MHD flow and heat transfer over a porous shrinking surface with velocity slip and temperature jump," *Math. Comput. Modell.*, vol. 56, no. 5–6, pp. 133–144, 2012. DOI: 10.1016/j.mcm.2011.11.080.

[20] M. E. Yazdi, A. Moradi and S. Dinarvand, "MHD mixed convection stagnation-point flow over a stretching vertical plate in porous medium filled with a nanofluid in the presence of thermal radiation" *Arab. J. Sci. Eng.*, vol. 39, no. 3, pp. 2251–2261, 2014. DOI: 10.1007/s13369-013-0792-x.

[21] A. Mirzaei, P. Jalili, M. D. Afifi, B. Jalili and D. D. Ganji, "Convection heat transfer of MHD fluid flow in the circular cavity with various obstacles: finite element approach," *Int. J. Thermofluids*, vol. 20, pp. 100522, 2023. DOI: 10.1016/j.ijft.2023.100522.

[22] M. Sagheer, I. Rashid, S. Hussain and M. Q. Khan, "The consequence of heat radiation on mhd flow of carreau nanofluid on a nonlinear stretchable surface with chemical process" *Int. J. Mod. Phys. B*, vol. 38, no. 10, pp. 2450147, 2024. DOI: 10.1142/S0217979224501479.

[23] J. B. J. Fourier, "Théorie analytique de la chaleur," *Gauthier-Villars*, vol. 1, pp. 354-365, 1888. DOI: 10.1016/B978-044450871-3/50107-8.

[24] C. Cattaneo, "Sulla conduzione del calore," *Atti Sem. Mat. Fis. Univ. Modena*, vol. 3, pp. 83–101, 1948. DOI: 10.1007/978-3-642-11051-1-5.

[25] C. I. Christov, "On frame indifferent formulation of the Maxwell–Cattaneo model of finite-speed heat conduction," *Mech. Res. Commun.*, vol. 36, no. 4, pp. 481–486, 2009. DOI: 10.1016/j.mechrescom.2008.11.003.

[26] H. Chen, Y. Ma, M. Shen, P. He and H. Zhang, "Significance of Cattaneo-Christov double diffusion and induced magnetic field on Maxwell ternary nanofluid flow with magnetic response boundary," *J. Magnet. Magnet. Mater.*, vol. 587, pp. 171264, 2023. DOI: 10.1016/j.jmmm.2023.171264.

[27] S. A. Lone, S. Anwar, S. Shahab, S. Iftikhar, A. Saeed and A. M. Galal, "Active and passive control of Casson nanofluid flow on a convectively heated nonlinear stretching permeable surface with the Cattaneo–Christov double diffusion theory," *Numer. Heat Transf. B Fundamental.*, vol. 85, no. 6, pp. 757–775, 2024. DOI: 10.1080/10407790.2023.2256969.

[28] C. K. G, B. P. Mallikarjun, S. Ghosh and S. Bhattacharyya, "Entropy analysis for two-dimensional double-diffusive mixed convective flow of a Williamson nanofluid through a porous medium," *Numer. Heat Transf. B Fundamental.*, pp. 1–21, 2024. DOI: 10.1080/10407790.2024.2329256.

[29] E. N. Thabet, A. M. Abd-Alla, H. A. Hosham and S. M. M. El-Kabeir, "Cattaneo-Christov heat and mass fluxes model of Casson fluid employing non-fourier double diffusion theories with ion slip and hall effects," *Ain Shams Eng. J.*, vol. 15, no. 4, pp. 102618, 2024. DOI: 10.1016/j.asej.2023.102618.

[30] B. Abu-Hijleh, M. Abu-Qudais and E. Abu Nada, "Numerical prediction of entropy generation due to natural convection from a horizontal cylinder," *Energy*, vol. 24, no. 4, pp. 327–333, 1999. DOI: 10.1016/S0360-5442(98)00103-0.

[31] E. Abu-Nada, "Numerical prediction of entropy generation in separated flows," *Entropy*, vol. 7, no. 4, pp. 234–252, 2005. DOI: 10.3390/e7040234.

[32] S. Chen, H. Han, Z. Liu, J. Li and C. Zheng, "Analysis of entropy generation in non-premixed hydrogen versus heated air counter-flow combustion," *Int. J. Hydrogen Energy*, vol. 35, no. 10, pp. 4736–4746, 2010. DOI: 10.1016/j.ijhydene.2010.02.113.

[33] R. Ellahi, M. Hassan and A. Zeeshan, "A study of heat transfer in power law nanofluid" *Therm. Sci.*, vol. 20, no. 6, pp. 2015–2026, 2016. DOI: 10.2298/TSCI150524129E.

[34] S. Hussain, K. Mehmood, M. Sagheer and M. Yamin, "Numerical simulation of double diffusive mixed convective nanofluid flow and entropy generation in a square porous enclosure," *Int. J. Heat Mass Transf.*, vol. 122, pp. 1283–1297, 2018. 122- DOI: 10.1016/j.ijheatmasstransfer.2018.02.082.

[35] M. I. Afridi and M. Qasim, "Entropy generation and heat transfer in boundary layer flow over a thin needle moving in a parallel stream in the presence of nonlinear Rosseland radiation," *Int. J. Thermal Sci.*, vol. 123, pp. 117–128, 2018. DOI: 10.1016/j.ijthermalsci.2017.09.014.

[36] M. K. Nayak, S. Shaw, H. Waqas and T. Muhammad, "Numerical computation for entropy generation in Darcy-Forchheimer transport of hybrid nanofluids with Cattaneo-Christov double-diffusion" *HFF*, vol. 32, no. 6, pp. 1861–1882, 2021. DOI: 10.1108/HFF-04-2021-0295.

[37] M. I. Khan, S. Qayyum, T. Hayat, M. I. Khan, A. Alsaedi and T. A. Khan, "Entropy generation in radiative motion of tangent hyperbolic nanofluid in presence of activation energy and nonlinear mixed convection," *Phys. Lett. A*, vol. 382, no. 31, pp. 2017–2026, 2018. DOI: 10.1016/j.physleta.2018.05.021.

[38] S. Hussain, M. Zeeshan and D. S. Sagheer, "Irreversibility analysis for the natural convection of Casson fluid in an inclined porous cavity under the effects of magnetic field and viscous dissipation," *Int. J. Thermal Sci.*, vol. 179, pp. 107699, 2022. DOI: 10.1016/j.ijthermalsci.2022.107699.

[39] A. Tanveer, M. B. Ashraf and M. Masood, "Entropy analysis of peristaltic flow over curved channel under the impact of mhd and convective conditions," *Numer. Heat Transf. B Fundamental.*, vol. 85, no. 1, pp. 45–57, 2024. DOI: 10.1080/10407790.2023.2224507.

[40] M. Bilal, M. Ramzan, Y. Mehmood, M. K. Alaoui and R. Chinram, "An entropy optimization study of non-Darcian magnetohydrodynami Williamson nanofluid with nonlinear thermal radiation over a stratifie sheet," *Proc. Inst. Mech. Eng. E J. Proc. Mech. Eng.*, vol. 235, no. 6, pp. 1883–1894, 2021. DOI: 10.1177/09544089211027989.

[41] Y. Chu, F. Shah, M. I. Khan, S. Farooq, S. Kadry and Z. Abdelmalek, "Investigation of viscous dissipation and entropy generation in third grade nanofluid flow over a stretched Riga plate with Cattaneo-Christov Double Diffusion (CCDD) model" *Phys. Scr.*, vol. 95, no. 11, pp. 115004, 2020. DOI: 10.1088/1402-4896/abbaf5.